CRS4

Centro di Ricerca, Sviluppo e
Studi Superiori in Sardegna
Uta - (CA)

Programma ENEA-MURST

Obiettivo 6

Validazione e rilascio del codice ARES

by:

M. Talice, S. Chibbaro and M. Mulas
Computational Fluid Dynamics Area

Contents

1 Test Case Description **3**

2 Numerical Simulations **5**

3 Results **8**

4 Discussion **17**

5 Further investigation **19**
5.1 Non adiabatic TFC model with adiabatic walls 20
5.2 Non adiabatic TFC model with isothermal walls 26

6 Sensitivity to turbulence models **32**

7 Conclusions **37**

References **38**

Abstract

This report concludes the activities of the second year of the project. During the second year a variety of turbulence models together with a partially premixed combustion model were developed [1], [2]. Implementation of the models into the new **Ares** combustion code and their validation was the objective of the present report. To the authors' knowledge however, there are no partially premixed benchmarks available in the literature, so that a thorough validation of this issue has to be postponed to the final year.

The test case proposed has been presented in the First European Test for Combustion Modeling Workshop, 1995 Aussois France [3], by the *Laboratoire de Combustion et Detonique de l'ENSMA* (hereinafter referred as ENSMA). This test case is appealing because even though it is geometrically simple, it reproduces the main features that can occur in actual industrial combustors.

It is a well known fact that premixed flames are unstable, therefore, in order to be used in practical applications they have to be stabilized. This is usually done by inducing the presence of stationary vortexes into the main flow in order to anchor the flame. A simple way to achieve this result is to put an obstacle inside the combustion chamber. The actual geometrical configurations used in the industrial combustors are complex and experimental measurements are not easy to be found.

The test case is described in Chapter I. In Chapeter II the most relevant parameters used for the computations are indicated. Chapter III presents the results which have been obtained.

The results show that the original TFC model formulation is not sufficient to provide good quantitative and also qualitative results in terms of temperature and velocity fields. The reason of such a failure has been investigated using also the **Fluent** code, as illustrated in Chapter IV. The thorough comprehension of deficiencies of the combustion model led to partial rescheduling of the third and final year of the project, during which the development of a non adiabatic version of the TFC model will be carried out.

Finally, in Chapter V, given the fact that combustion and turbulence are strongly coupled, the sensitivity of the results to different turbulence models has been evaluated. In particular, the second order closure turbulence model (Reynolds Stress Model) which is available in Fluent, has been tested.

1 Test Case Description

The experimental set-up is shown in figure 1, where a longitudinal section of the combustion chamber is represented.

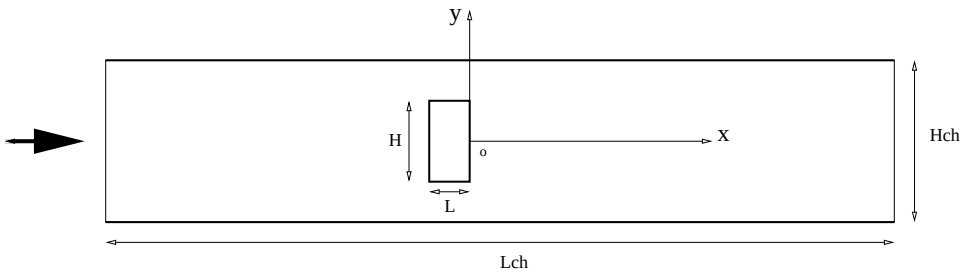

Figure 1: Test Case Geometry.

A premixed mixture of propane and air flows through a channel, where a square section bar has been inserted. The channel and obstacle dimensions are those reported in table 1

Channel			Obstacle		
$L_{\{ch\}}(mm)$	$H_{\{ch\}}(mm)$	$W_{\{ch\}}(mm)$	$L\,(mm)$	$H\,(mm)$	$W\,(mm)$
2200	28.8	160	5	9.6	160

Table 1: Geometric dimensions

For a hydrocarbon fuel given by C_xH_y, the stoichiometric reaction can be written as:

$$C_xH_y + a(O_2 + 3.76N_2) \rightarrow xCO_2 + (y/2)H_2O + 3.76aN_2$$

where: $a = x + y/4$. The stoichiometric air to fuel ratio is given by:

$$(A/F)_{\{stoic\}} = \left(\frac{m_{\{air\}}}{m_{\{fuel\}}}\right) = \frac{4.76a}{1}\frac{MW_{\{air\}}}{MW_{\{fuel\}}}$$

where $MW_{\{air\}}$ and $MW_{\{fuel\}}$ are the molecular weight of air and fuel, respectively.

The temperature of the mixture at the inlet section is $273K$ and the mass-flow per unit of channel thickness is equal to $0.2722Kg/m/s$, corresponding to a maximum speed of the main flow of $8.2m/s$. The resulting Reynolds number based on the channel height is $Re = 17810$, whereas the corresponding value based on the obstacle height is $Re = 5937$.

The chemical reaction which describes the combustion process is given by:

$$\Phi C_3H_8 + 5\,(O_2 + 3.76N_2) \rightarrow \Phi CO_2 + 4\Phi H_2O + (5 - 5\Phi)\,O_2 + 18.8N_2 \qquad (1)$$

equivalence ratio	Φ	0.65
fuel mass fraction	$Y_{C_3H_8}$	0.04
oxygen mass fraction	Y_{O_2}	0.2237
nitrogen mass fraction	Y_{N_2}	0.7363
mixture temperature	T_{unb} [K]	273.0
mixture density	ρ_{unb}	1.3059
adiabatic flame temperature	T_{adiab}[K]	1780.0
specific heat	C_P	1614
heat of combustion	H_{comb} [J/kg]	50×10^6

Table 2: Mixture composition and properties

The mixture composition together with other quantities of interest are reported in table 2, where the equivalence ratio Φ of the mixture is expressed by:

$$\Phi = \frac{(A/F)_{\{stoic\}}}{(A/F)}$$

Measurements are available for non-reactive and reactive flow conditions and the description of the experimental results can be found in reference [3]. The experiments have found the evidence of the existence of two vortexes downstream the obstacle. The effect of this recirculation zone is the stabilization of the flame. The longitudinal extension of the recirculation zone has been measured to be equal to $4x/H$ along the combustor axis.

2 Numerical Simulations

The numerical simulation of the ENSMA test case has been carried out by using the codes ARES and Fluent. The two codes have been run using, as far as possible, the same conditions, such as numerical schemes, physical models and computational grid.

Figure 2 shows the grid topology of the 4-block mesh used, and an enlargement of the computational domain around the obstacle. In the same figure, the positions of the three cross-sections on which experimental data are available, are also shown. In order to assure grid independence results, the computations have been repeated by using two finer meshes which are obtained by doubling the number of cells of the coarse grid. Table 3 gives the number of cells used in the x and y directions for each block and for each grid level. Results obtained with grid level B de facto match those obtained with grid level C, and will be the only ones reported in the following.

As previously mentioned, the stabilization of the flame behind the flame holder is due to the presence of two vortexes. Hence, a correct description of the turbulent flow behavior is a critical issue of the test case simulation. The turbulence models which have been used were the two models of the $\kappa - \epsilon$ family, namely standard and RNG, plus the $\kappa - log(\omega)$ model. The Fluent computations have been carried out by making use of the $\kappa - \epsilon$ family models only, because the $\kappa - log(\omega)$ model was not available in the version 5.5 of the code. The Spalart and Allmaras one-equation turbulence model which has been implemented into the ARES code, has not been used in the simulation. In fact, an intrinsic limitation of that model is that it is not possible to clearly assign the incoming flow a chosen turbulence intensity (or a given profile of turbulent kinetic energy). The validation of the model is hence postponed to a successive task. Inlet profiles (transversal distributions) for the average quantities $\overline{u}, \overline{\kappa}$ and $\overline{\varepsilon}$ have been imposed at the inlet section and are those reported in figures 3 and 4. The value of $\overline{\kappa}$ and $\overline{\varepsilon}$ have been computed from the measured profiles of $\sqrt{u'^2}$ and $\sqrt{v'^2}$ by using relations:

$$\kappa = \frac{1}{2}\left(\sqrt{u'^2} + 2. * \sqrt{v'^2}\right) ; \qquad \varepsilon = -c_\mu \frac{\kappa^2}{\overline{uv}} \frac{\partial \overline{u}}{\partial y}$$

In the case of the $\kappa - log(\omega)$ model, the $log(\omega)$ profile has been imposed at the inlet section. It can been computed from the corresponding κ and ϵ ones by using the relation:

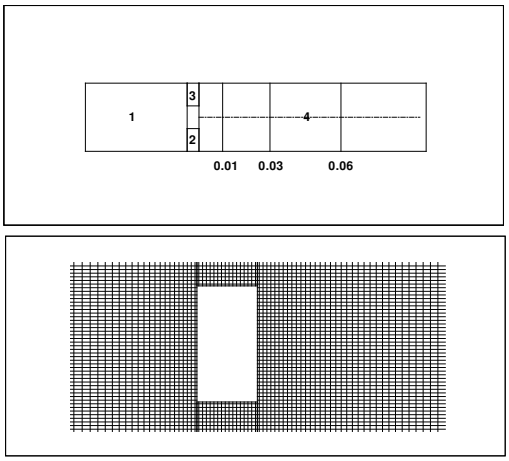

Figure 2: Blocks topology (up); mesh detail around the obstacle (bottom)

	Level A			Level B			Level C		
Bl	Nl	NJ	Cells	Nl	NJ	Cells	Nl	NJ	Cells
1	48	96	4608	96	192	18432	192	384	73728
2	32	64	2048	64	128	8192	128	256	32768
3	32	64	2048	64	128	8192	128	256	32768
4	96	96	9216	192	192	36864	384	384	147456
			17920			71680			286720

Table 3: Mesh size

$$log(\omega) = log\left(\frac{\epsilon}{C_{\mu}\kappa}\right)$$

Wall functions have been used at solid walls. At the outlet section, the pressure value of 101325 [Pa] has been imposed.

The TFC premixed combustion model has been used for the present computation. An exhaustive description of the model could be found in [4] and [5]. The inlet value of the progress variable $\tilde{c}$ has been set to zero (unburned mixture).

The QUICK spatial discretization scheme has been used for both ARES and FLUENT computations. The linear system integration method used in the ARES code was the BICGSTAB, preconditioned by using the ADI algorithm. In the Fluent case, the SEGREGATED solver has been used, with the default options.

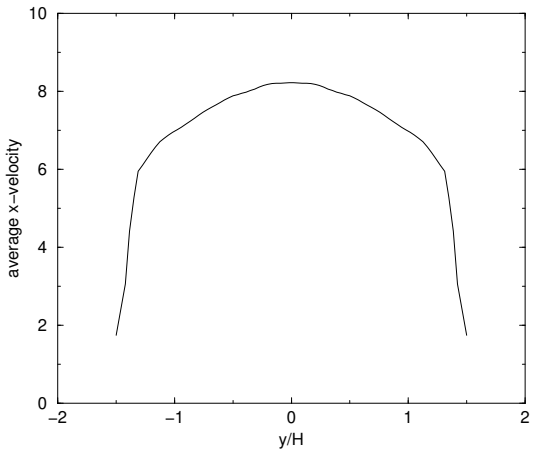

Figure 3: x-velocity distribution at inlet

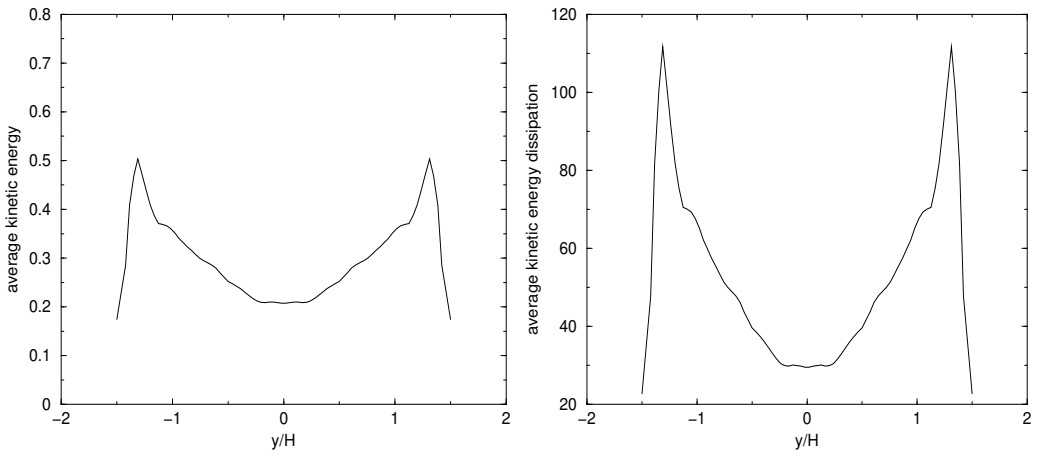

Figure 4: κ and ϵ

3 Results

In the figures 5 and 6 the normalized residuals of the resolved equations are reported. Both codes have been started from the coarser grid level solution. Convergence has to be considered at a more than satisfactory level and no significant modification of the obtained solutions have been found after some extra 100 iterations.

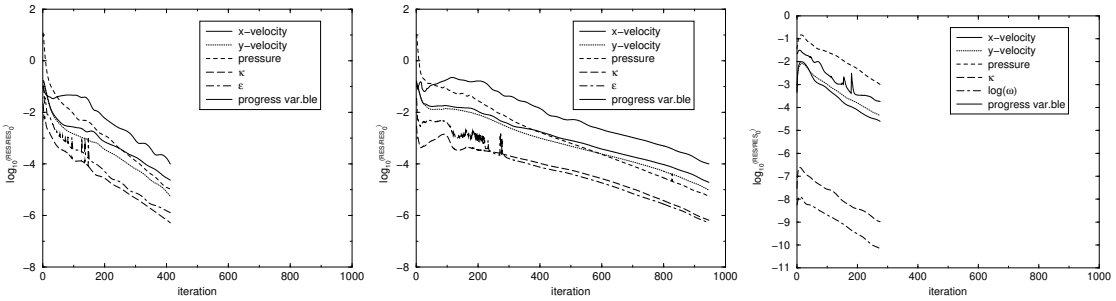

Figure 5: Ares: convergence history; $\kappa - \epsilon$ left; RNG $\kappa - \epsilon$ center; $\kappa - log(\omega)$ right

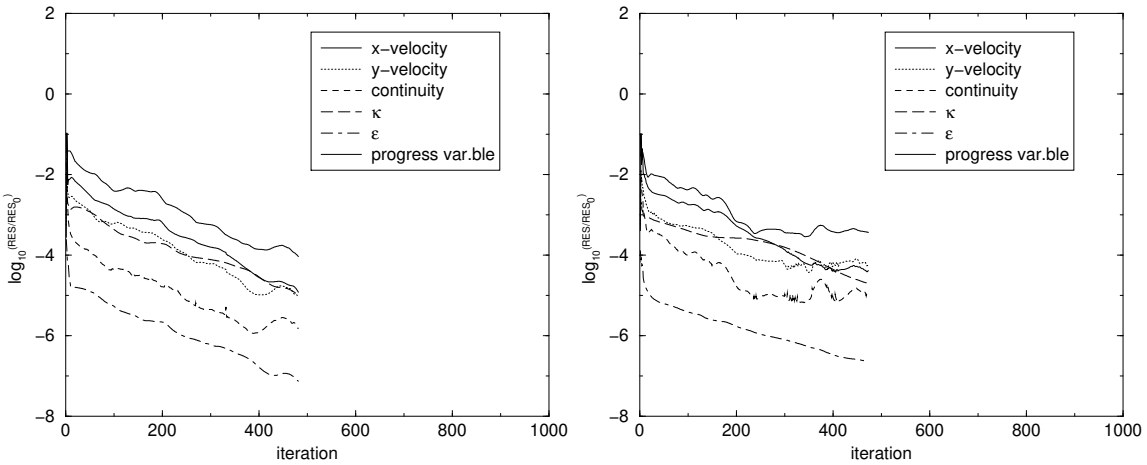

Figure 6: Fluent: convergence history; $\kappa - \epsilon$ left; RNG $\kappa - \epsilon$

Figure 7 shows the computed progress variable $\tilde{c}$ contour plots together with the streamlines for **Ares** calculations. The figures 8 and 9 show the computed progress variable $\tilde{c}$ contour plots for **Fluent** calculations.

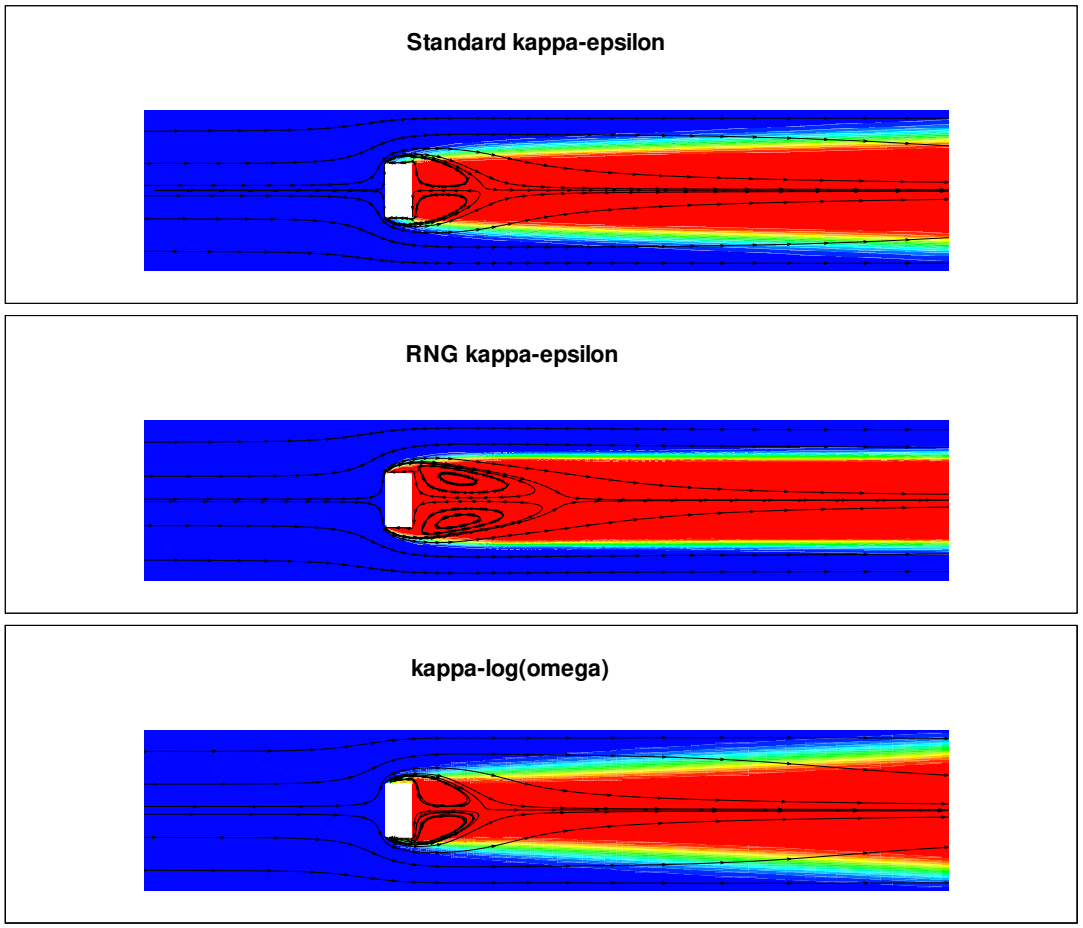

Figure 7: Ares: progress variable contour plots;

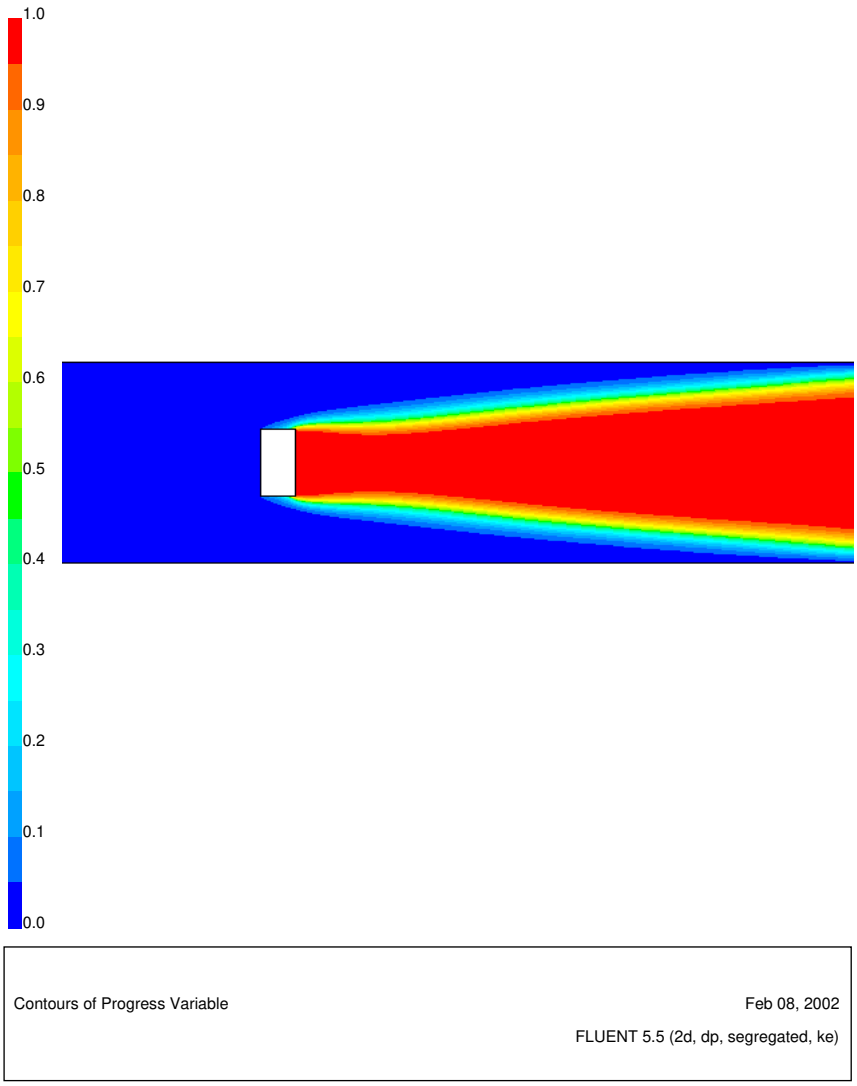

Figure 8: Fluent: progress variable contour plot; $\kappa - \epsilon$

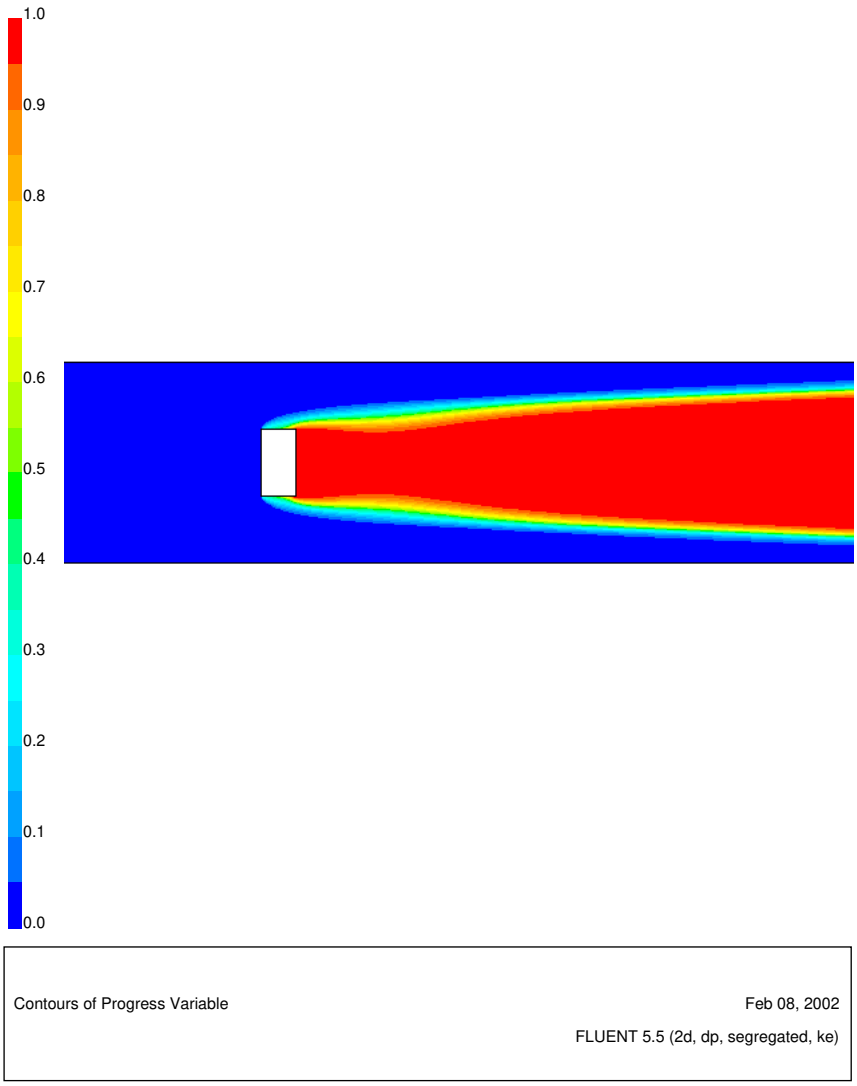

Figure 9: Fluent: progress variable contour plot; RNG $\kappa - \epsilon$

The figures 10, 11 and 12 show the comparison of the computed temperature profiles to the experimental data at $x/H = 1.04167$, 3.125 and 6.25 from the obstacle.

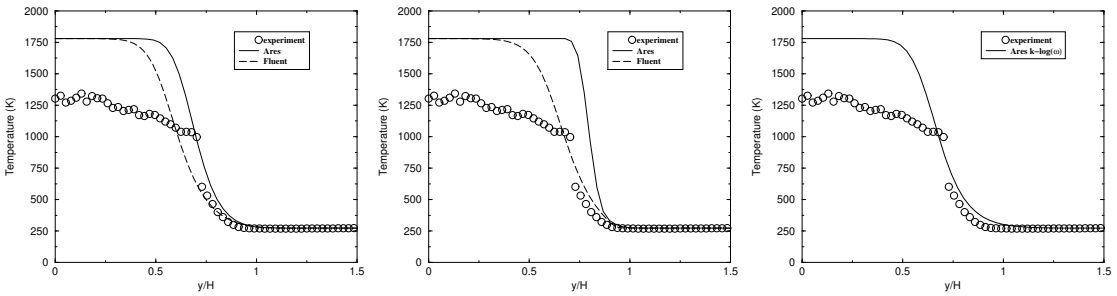

Figure 10: Temperature profile at $x/H = 1.04167$; $\kappa - \epsilon$ left; RNG $\kappa - \epsilon$ center; $k - log(\omega)$ right.

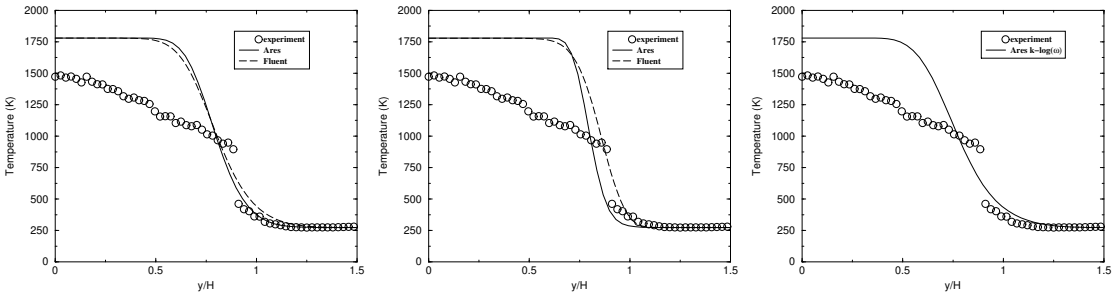

Figure 11: Temperature profile at $x/H = 3.125$; $\kappa - \epsilon$ left; RNG $\kappa - \epsilon$ center; $k - log(\omega)$ right.

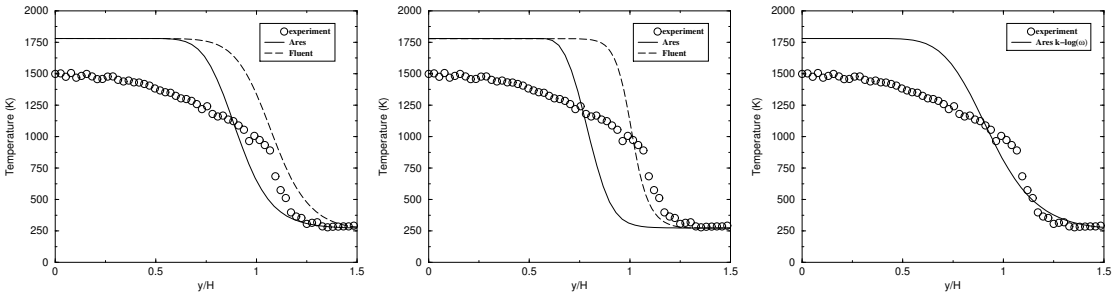

Figure 12: Temperature profile at $x/H = 6.25$; $\kappa - \epsilon$ left; RNG $\kappa - \epsilon$ center; $k - log(\omega)$ right.

The figures 10, 11 and 12 show a substantial agreement between **Ares** and **Fluent** results. The difference between the computed and the experimental temperature is about 400 K at the section nearest to the obstacle and about 280 K at the two sections further downstream.

However, it must be reminded here that, when using the TFC model, the temperature represents a quantity derived from the calculated progress variable $\tilde{c}$ as:

$$T = T_b \tilde{c} + T_u (1. - \tilde{c}) \tag{2}$$

and what it is actually shown in the pictures is the progress variable.

Figure 13, shows the distribution of the streamwise velocity component along the combustor axis. The true measured ricirculation region can be clearly compared to the calculated ones, previously shown in figure 7.

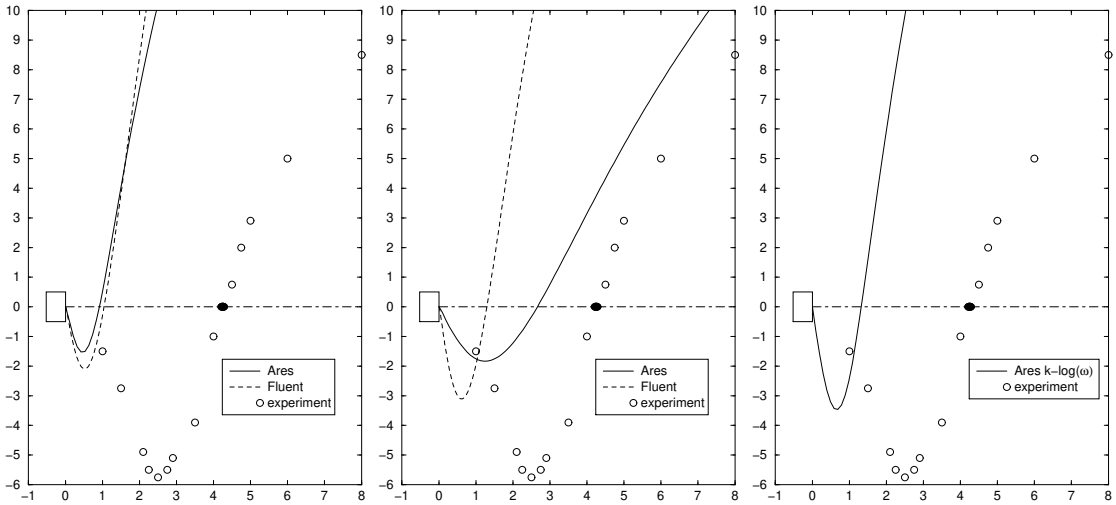

Figure 13: x-velocity distribution along the combustor axis; $\kappa - \epsilon$left; RNG $\kappa - \epsilon$ center; $k - log(\omega)$ right.

Profiles of streamwise and crosswise components of the velocity are shown in figures 14, 15, 16 and 17, 18, 19 respectively.

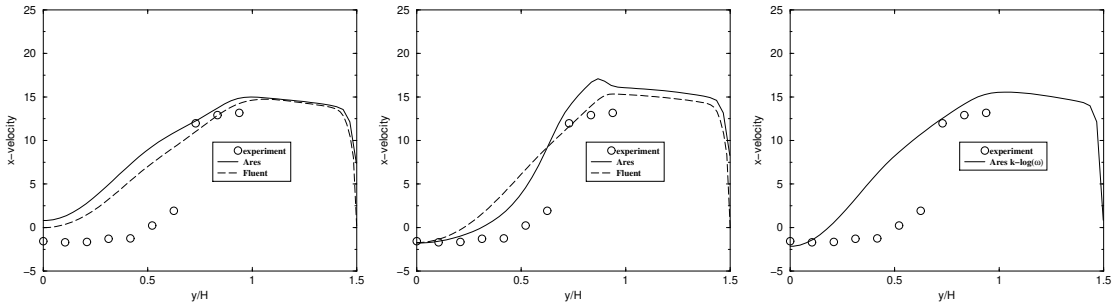

Figure 14: x-velocity profile at $x/H = 1.04167$; $\kappa - \epsilon$ left; RNG $\kappa - \epsilon$ center; $k - log(\omega)$ right.

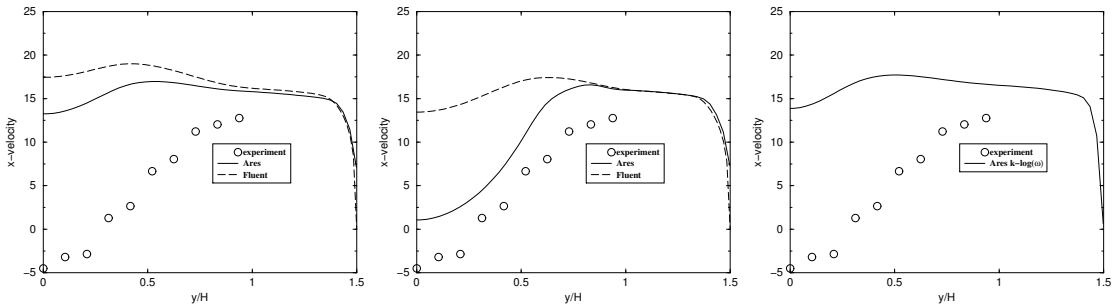

Figure 15: x-velocity profile at $x/H = 3.125$; $\kappa - \epsilon$ left; RNG $\kappa - \epsilon$ center; $k - log(\omega)$ right.

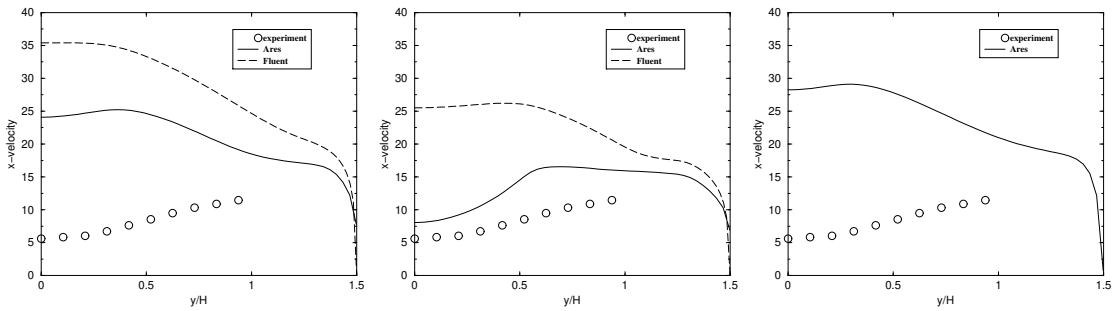

Figure 16: x-velocity profile at $x/H = 6.25$; $\kappa - \epsilon$ left; RNG $\kappa - \epsilon$ center; $k - log(\omega)$ right.

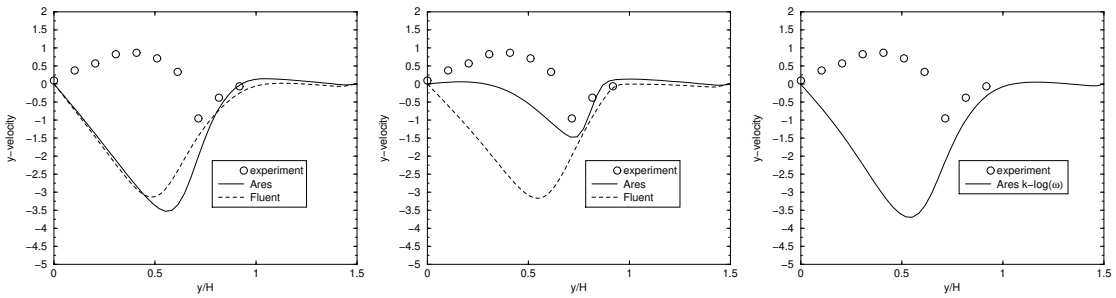

Figure 17: y-velocity profile at $x/H = 1.04167$; $\kappa - \epsilon$ left; RNG $\kappa - \epsilon$ center; $k - log(\omega)$ right.

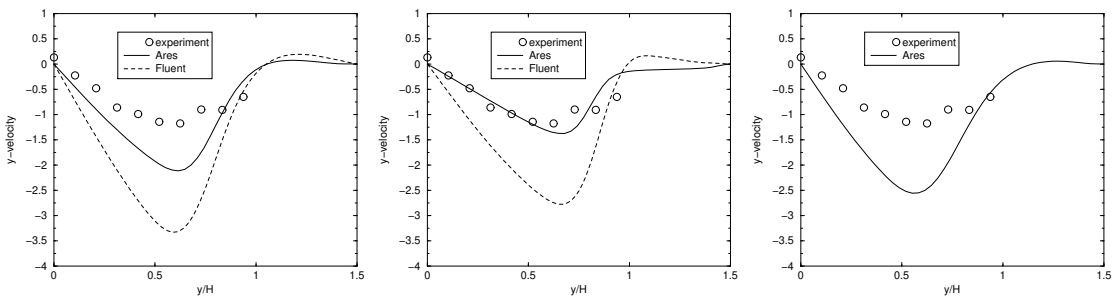

Figure 18: y-velocity profile at $x/H = 3.125$; $\kappa - \epsilon$ left; RNG $\kappa - \epsilon$ center; $k - log(\omega)$ right.

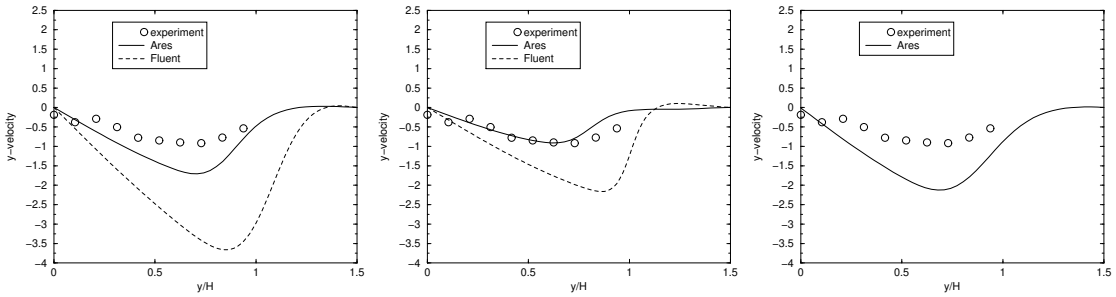

Figure 19: y-velocity profile at $x/H = 6.25$; $\kappa - \epsilon$ left; RNG $\kappa - \epsilon$ center; $k - log(\omega)$ right.

Finally, the figure 20 shows the profiles of turbulent kinetic energy at $x/H = 1.04167$. The ARES RNG $\kappa - \epsilon$ model provides a general good agreement with experimental data, even though the maximum value appears underestimated.

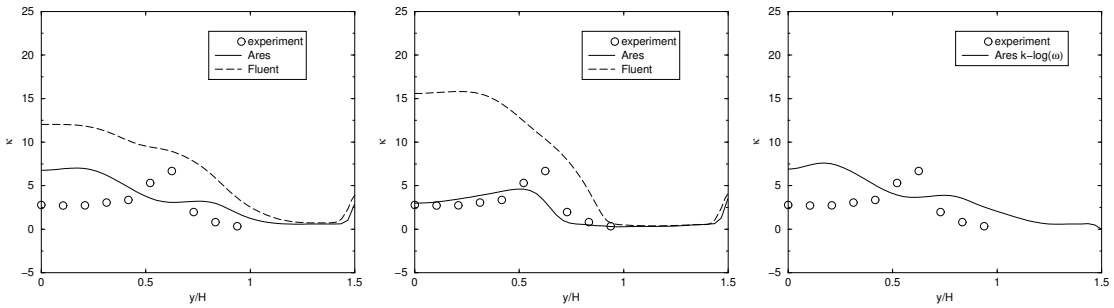

Figure 20: turbulent kinetic energy profile at $x/H = 1.04167$; $\kappa - \epsilon$ left; RNG $\kappa - \epsilon$ center; $k - log(\omega)$ right.

4 Discussion

From the analysis of the pictures shown in the previous section some issues deserve further investigation and better comprehension:

[1] dimension of ricirculating region behind the obstacle

it is strongly underestimated; a remarkable exception is represented by the simulation produced by the RNG $\kappa - \epsilon$ model implemented into **Ares**;

[2] streamlines pattern and velocity fields downstream

profiles of crosswise velocity components far downstream of the obstacle suggest that the streamlines do not bend toward the combustor axis, as found by most of the calculations; again the RNG model of **Ares** gives the correct qualitative behaviour;

[3] temperature level

all models predict a temperature level, right behind the obstacle, given by the adiabatic flame temperature which, as a matter of fact, overestimates of about 400 K the measured level; in reference [3] it is suggested a power loss through the solid bar due to heat conduction; moreover, the temperature measures show a minimum level (about 1250 K) upstream, with respect to about 1500 K downstream, which can be explained only by assuming a certain level of instability of the vorteces behind the obstacle which in turn may allow fresh mixture to be entrained;

[4] flame opening

Ares RNG results determine the least degree of flame opening, also compared to **Fluent** RNG results; the $\kappa - log(\omega)$ results show the maximum level, followed by the standard $\kappa - \epsilon$;

[5] temperature profiles

this issue is tightly connected to the previous one due to the temperature relation to the progress variable: all models fail to reproduce the slope of the temperature profiles; apparently the worst slope is that produced by **Ares** RNG model, which is the steepest one: this is in contradiction to the previous comments about the RNG results by **Ares**;

[6] effects of turbulence model

turbulence modelling seems to play a fundamental role for the correct simulation of the ricirculating vorteces and the flame front opening as well;

[7] **Ares** versus **Fluent**

though the results of the two codes are very similar to each other, **Ares** gives better results in almost all situations, and particularly when the RNG turbulence model is used.

As reminded previously in the text, the temperature versus the progress variable relation must also be taken into acount when discussing the results. The TFC model, as developed and implemented into **Ares** code, is adiabatic and non heat-conducting. The model is adiabatic because, since $T = T(\tilde{c})$, only the progress variable equation is solved, with Neumann wall boundary conditions. As a result, no isothermal wall conditions can ever be used, and the suggested heat loss through the conductiong bar, cannot be simulated. The model is also non heat conducting because there is no way to diffuse internal energy in a stream of burned gases ($\tilde{c} = 1$). In other words, a burned stream cannot be cooled, which represents a model limitation.

Whether the heat conduction loss through the walls, or the heat diffusion within the burned stream of gas, or both of them, are responsible for the lower temperatures, the computed density fields are much lower than the measured ones and, as a consequence, the velocity fields are also affected due to the continuity equation. The higher velocity levels might in turn interact with the turbulence model and generate at the end a much smaller ricirculating region. In other words, there is a chain reaction of effects that must be understood. The better behaviour of the **Ares** RGN turbulence model might, in the end, have been determined by chance only.

If it is true that a major failure is determined by the adiabatic and non heat conducting character of the TFC model, then a model upgrade is needed and the combustion model extension to heat conducting case must be scheduled in the third and final year of the project. In the following sections, **Fluent** non adiabatic TFC model is used to investigate further the ENSMA test case.

5 Further investigation

The examination of the experimental results shows that the actual flow field is characterized by a stream of high temperature combustion products surrounded by a stream of cold mixture. Moreover the exchange of thermal energy throughout solid walls should be taken into account. In fact, even ignoring the heat flow through the external walls seems reasonable enough, the hypothesis of adiabaticity couldn't be applied to the obstacle walls. In other words, two mechanisms are to be put in evidence, by which thermal energy is transfered:

- thermal energy is *diffused* from hot to cold mixture;
- thermal energy is drained out the system throughout the obstacle walls due to *conduction*.

The necessity of including somehow energy into the mathematical model in order to get a more accurate description of the physical behavior of the system, suggested to make use of the non adiabatic version of the TFC model which is available in **Fluent**. A complete description of the model can be found in [6]. In the scope of the present work it is only important to remind that, accordingly to the non adiabatic formulation, the energy equation, written in terms of static enthalpy, is solved together with the progress variable equation, being the chemical source term in the energy equation proportional via the heat of combustion H_{comb} and the fuel mass fraction Y_f, to the $\tilde{c}$ equation source term and being the local density computed as:

$$\rho = \frac{\rho_u T_u}{T}$$

where the temperature T is derived from the energy equation and calculated as:

$$T = \frac{h}{c_p}$$

instead of:

$$T = T_{ad}\tilde{c} + T_u(1 - \tilde{c})$$

as in the adiabatic TFC model.

In order to weight the relative importance of the two previously mentioned mechanisms through which energy can be exchanged between hot and cold fluid regions and

between the fluid flow and solid walls, two sets of calculations have been carried out. At first, the non adiabatic version of the TFC model has been used, together with adiabatic condition at solid walls. So that, the only difference with the TFC simulation discussed in the previous chapter, was the version of the combustion model, only (non adiabatic vs adiabatic). Then, isothermal conditions have been applied to the solid wall limiting the computational domain. Thus, in this second set of simulation not only energy diffusion, but also the energy flow from the combustion chamber to the obstacle walls was taken into account. In order to be able to set a reasonable value for the obstacle wall temperature, the fully 3D coupled solid-fluid problem has been solved. Thermal energy can be exchanged between the obstacle and the external world via conduction. By the resolution of the 3D problem the correct temperature value to be assigned at the solid walls has been determined.

5.1 Non adiabatic TFC model with adiabatic walls

Figures 21, 22 and 23 show the temperature profiles at the 3 sections. Figures 24, 25 and 26 and figures 27, 28 and 29 show the streamwise and the crosswise velocity components respectively, at the same combustor sections. All figures compare the adiabatic to the non adiabatic model implemented in **Fluent**.

Maximum temperatures fall to about 1500 K when using the non adiabatic model, recovering the measured values, apart from the section closest to the obstacle. The crosswise velocity component at section $x/H = 1.04167$ doesn't seem to be effected too much by the errors made in the evaluation of the temperature field, showing no significant difference between the results obtained by using the two models. At the two remaining sections further downstream the channel, the effect of the energy diffusion becomes more evident, so that the maximum error made in the evaluation of the velocity is reduced by around 4 to 9 m/s depending on the turbulence model used and on the examined location.

Some improvement in the results could be also observed for the crosswise component of velocity. The most significant effects are found for the standard $\kappa - \epsilon$ model, for which the relative maximum error has been reduced up to about 30%.

As expected, the most relevant improvement on the results are obtained in the evaluation of the temperature field. The maximum level of the temperature is well captured by the model, as well as the flame front position and thickness. Diffusion in

the crosswise direction is still poorly evaluated compared to the measures, and might depend upon the turbulence model.

The examination of figures 30 and 31 shows no significant improvement in the resolution of both the turbulent kinetic energy and axial distribution of the longitudinal velocity component, by using the non adiabatic TFC model.

Apart from the better temperature level, these results remain poorer with respect to the best **Ares** results.

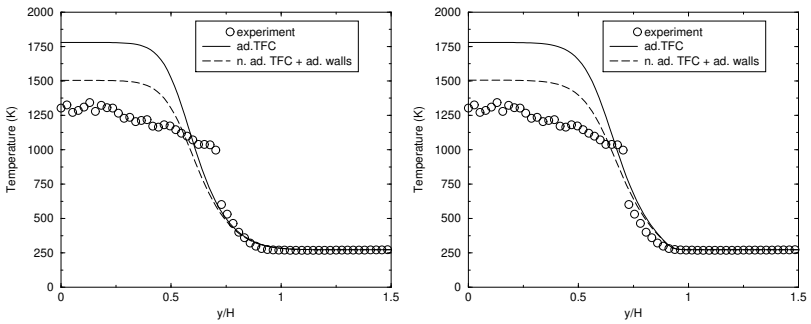

Figure 21: Adiabatic TFC vs non adiabatic TFC with adiabatic wall conditions: temperature profile at $x/H = 1.04167$; $\kappa - \epsilon$ left; RNG $\kappa - \epsilon$ right.

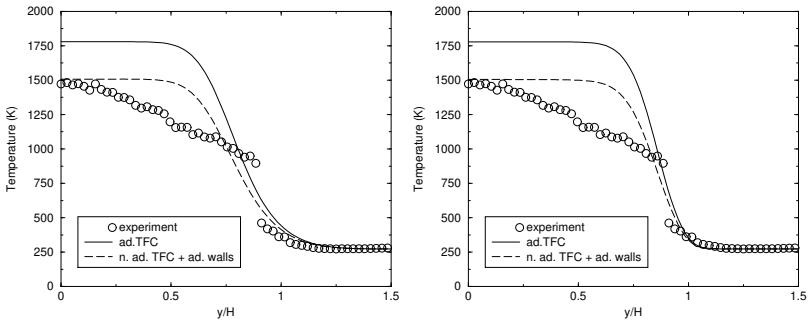

Figure 22: Adiabatic TFC vs non adiabatic TFC with adiabatic wall conditions: temperature profile at $x/H = 3.125$; $\kappa - \epsilon$ left; RNG $\kappa - \epsilon$ right.

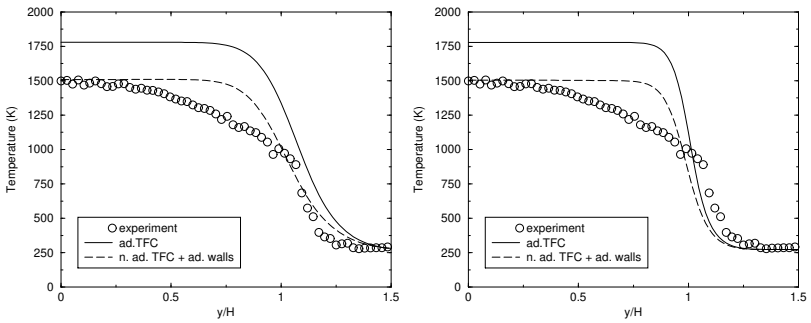

Figure 23: Adiabatic TFC vs non adiabatic TFC with adiabatic wall conditions: temperature profile at $x/H = 6.25$; $\kappa - \epsilon$ left; RNG $\kappa - \epsilon$ right.

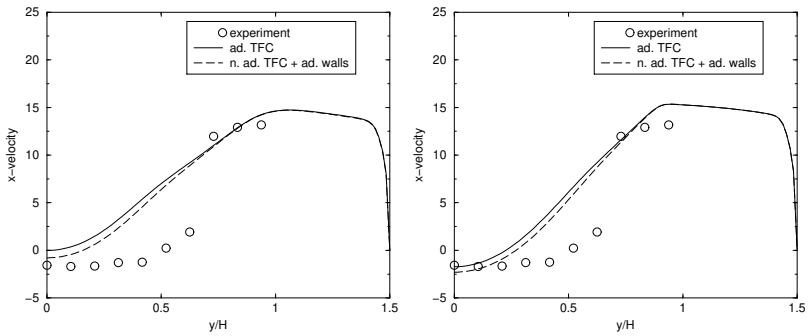

Figure 24: Adiabatic TFC vs non adiabatic TFC with adiabatic wall conditions: x-velocity profile at $x/H = 1.04167$; $\kappa - \epsilon$ left; RNG $\kappa - \epsilon$ right.

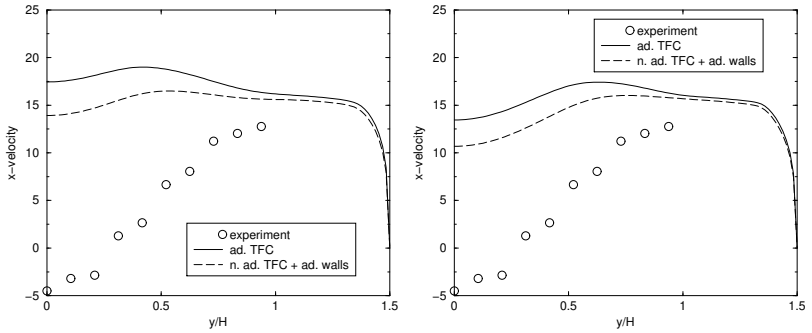

Figure 25: Adiabatic TFC vs non adiabatic TFC with adiabatic wall conditions: x-velocity profile at $x/H = 3.125$; $\kappa - \epsilon$ left; RNG $\kappa - \epsilon$ right.

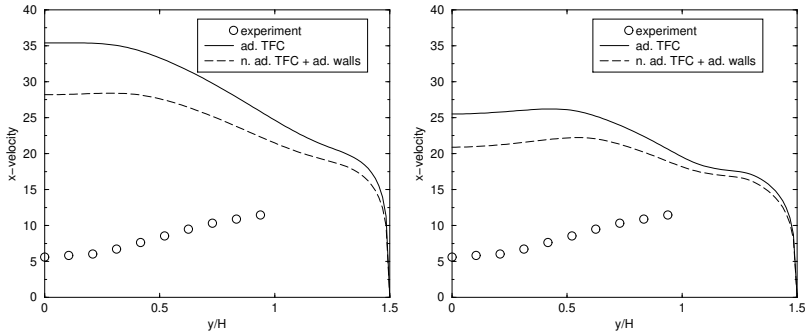

Figure 26: Adiabatic TFC vs non adiabatic TFC with adiabatic wall conditions: x-velocity profile at $x/H = 6.25$; $\kappa - \epsilon$ left; RNG $\kappa - \epsilon$ right.

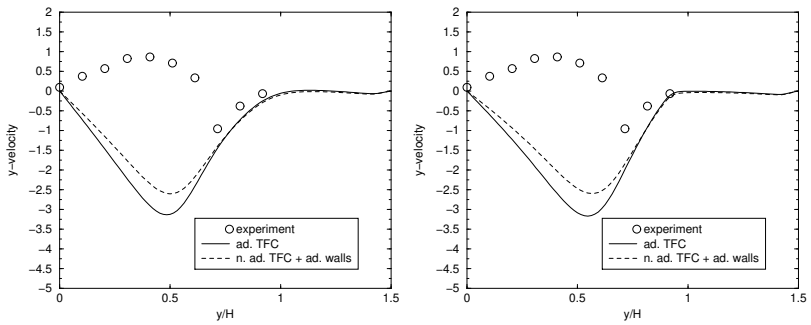

Figure 27: Adiabatic TFC vs non adiabatic TFC with adiabatic wall conditions: y-velocity profile at $x/H = 1.04167$; $\kappa - \epsilon$ left; RNG $\kappa - \epsilon$ right.

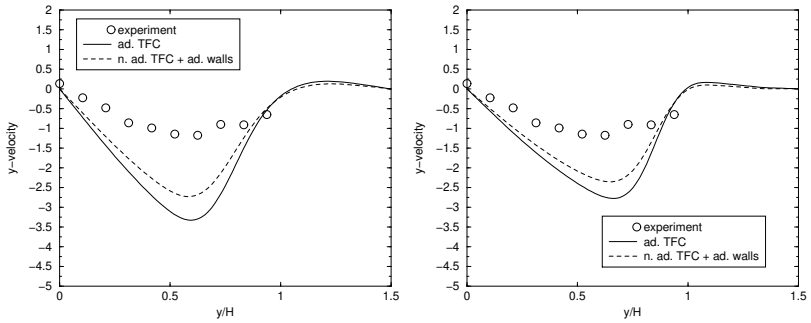

Figure 28: Adiabatic TFC vs non adiabatic TFC with adiabatic wall conditions: y-velocity profile at $x/H = 3.125$; $\kappa - \epsilon$ left; RNG $\kappa - \epsilon$ right.

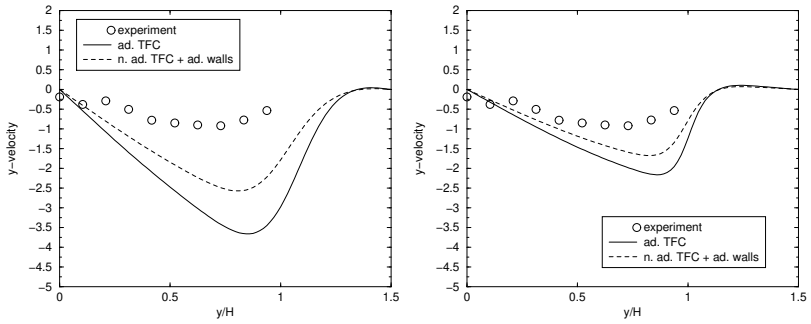

Figure 29: Adiabatic TFC vs non adiabatic TFC with adiabatic wall conditions: y-velocity profile at $x/H = 6.25$; $\kappa - \epsilon$ left; RNG $\kappa - \epsilon$ right.

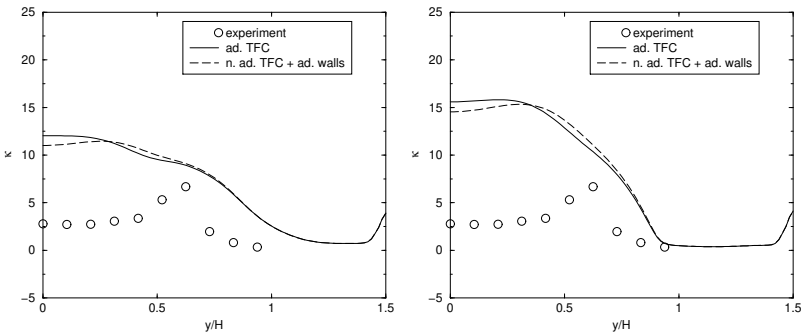

Figure 30: Adiabatic TFC vs non adiabatic TFC with adiabatic wall conditions: κ profile at $x/H = 1.04167$; $\kappa - \epsilon$ left; RNG $\kappa - \epsilon$ right.

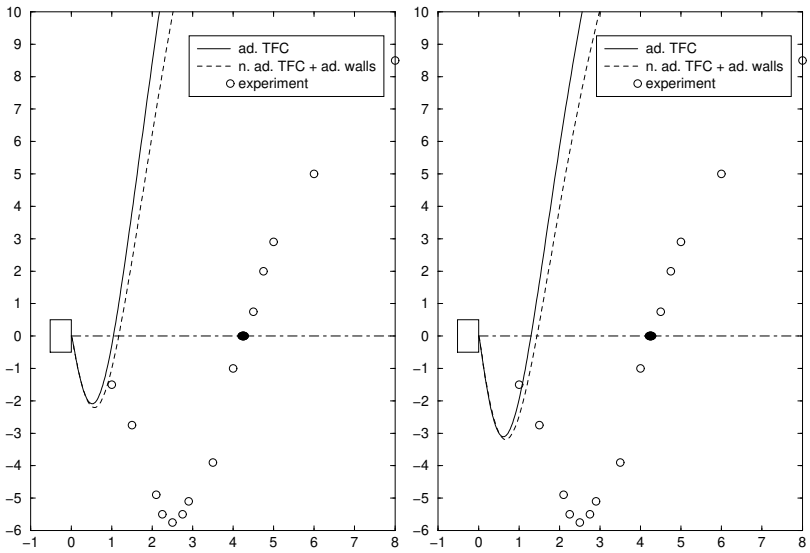

Figure 31: Adiabatic TFC vs non adiabatic TFC with adiabatic wall conditions: x-velocity distribution along the combustor axis; $\kappa - \epsilon$ left; RNG $\kappa - \epsilon$ right

5.2 Non adiabatic TFC model with isothermal walls

As mentioned before, the fully 3D coupled fluid - solid problem has been solved in order to determine the obstacle walls temperature. In fact, whereas it is straightforward to set the channel wall temperature at the same value of the cold flow stream, namely $273K$, nothing is known about the temperature which exists at the obstacle surface. In the experimental apparatus the obstacle is not cooled and it can exchange thermal energy with the external world by conduction only, its extremities being kept at the same temperature of the external walls. In absence of experimental data for the temperature distribution over the obstacle surface, the 3D fluid - solid coupled computation has been then carried out. The figure 32 shows the temperature contour plot over the obstacle surface and the temperature distribution along the obstacle axis. The exam of figure 32 suggests that far enough from the channel walls, the obstacle surface temperature assumes the quasi-constant value of 600 K across the channel width. This value has been imposed at the obstacle wall in all the 2D computations.

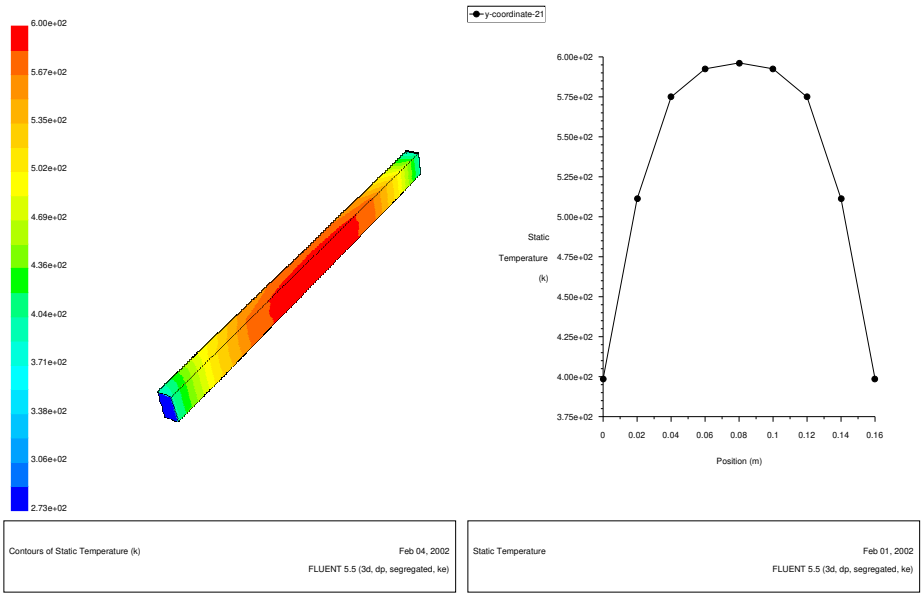

Figure 32: Temperature distribution over the obstacle surface (left) and along the obstacle axis (right).

The exam of figures 33 to 38 shows that no significant improvements have been achieved by replacing the adiabatic wall condition with the isothermal one in resolving

the flow velocity components. Also figures 42 and 43 don't reveal any important improvement of the results accuracy.

The only observed effects which have been obtained by using the isothermal conditions at solid walls, are on the temperature, especially at the section $x/H = 1.04167$, as shown in figure 39. The maximum temperature value has been lowered by about 20 K with respect to the corresponding value which was computed by the use of adiabatic conditions at solid walls. Hence, even though it has been proven that some effect exists on the temperature distribution due to the exchange of thermal energy between the flow and the obstacle wall (whose temperature has been evaluated to be around 600 K), nevertheless this mechanism of energy transfer is not such to justify the experimental value of temperature which has been measured at the section $x/H = 1.04167$. There must be some other more relevant physical mechanism which gives reason of such behavior. According to [3] it has been experimentally observed that the vortex system downstream the obstacle shows a pulsatile behavior, namely it moves back and forth along the channel axis. This movement could be responsible for the entrapment of gas at lower temperature in the zone right behind the obstacle, which would lead to a lower value of the average temperature. This effect, which is of strongly unsteady nature, has not been accounted for in anyway in the present simulation, which presents only stationary results.

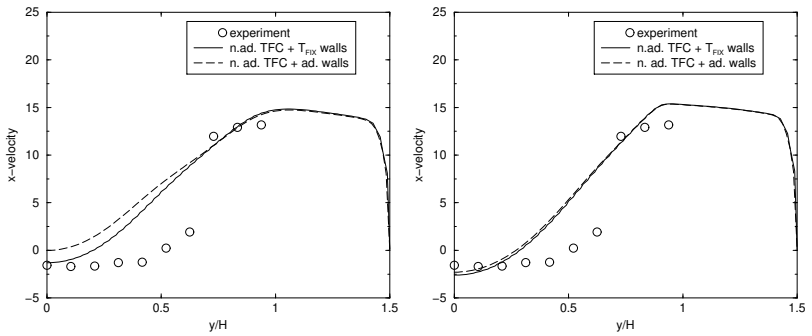

Figure 33: Adiabatic vs non adiabatic wall conditions: x-velocity distribution at $x/H = 1.04167$; $\kappa - \epsilon$ left; RNG $\kappa - \epsilon$ right.

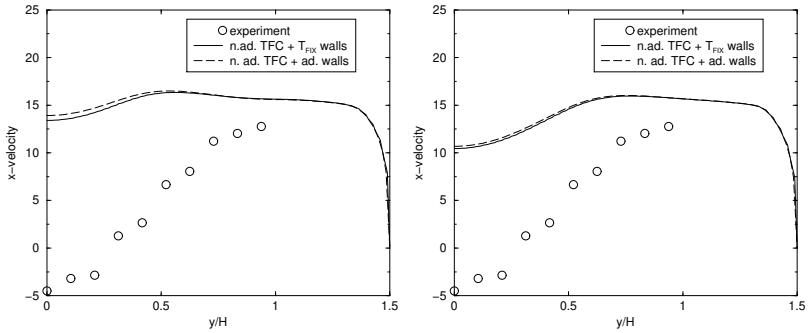

Figure 34: Adiabatic vs non adiabatic wall conditions: x-velocity distribution at $x/H = 3.125$; $\kappa - \epsilon$ left; RNG $\kappa - \epsilon$ right.

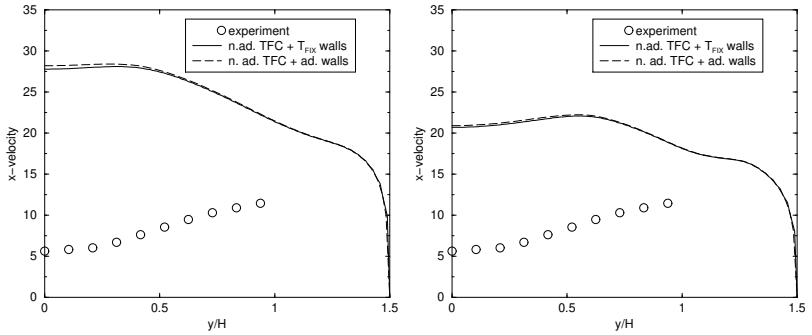

Figure 35: Adiabatic vs non adiabatic wall conditions: x-velocity distribution at $x/H = 6.25$; $\kappa - \epsilon$ left; RNG $\kappa - \epsilon$ right.

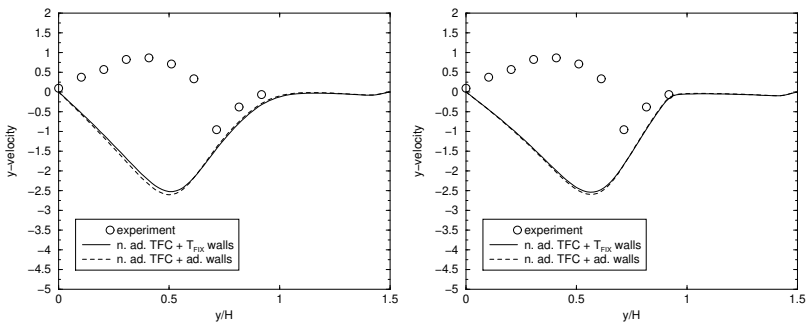

Figure 36: Adiabatic vs non adiabatic wall conditions: y-velocity distribution at $x/H = 1.04167$; $\kappa - \epsilon$ left; RNG $\kappa - \epsilon$ right.

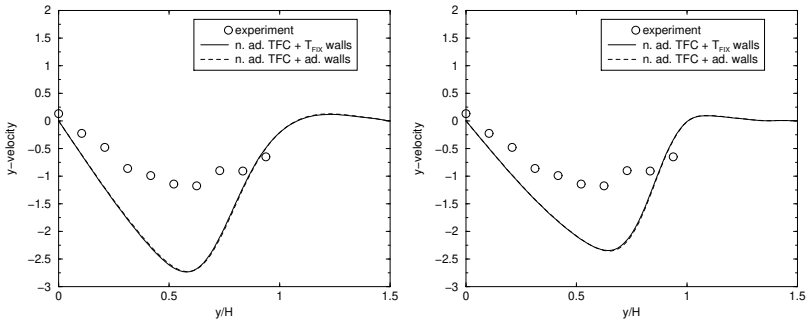

Figure 37: Adiabatic vs non adiabatic wall conditions: y-velocity distribution at $x/H = 3.125$; $\kappa - \epsilon$ left; RNG $\kappa - \epsilon$ right.

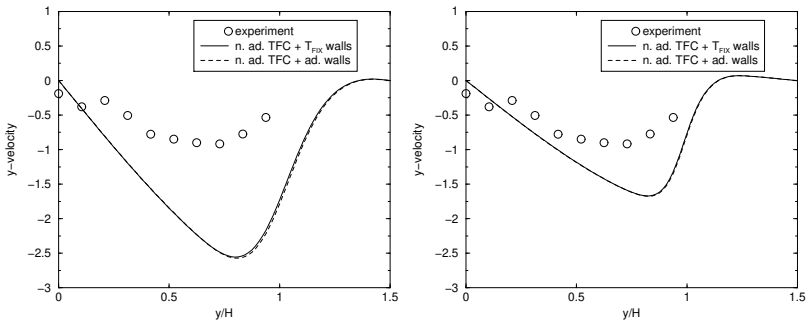

Figure 38: Adiabatic vs non adiabatic wall conditions: y-velocity distribution at $x/H = 6.25$; $\kappa - \epsilon$ left; RNG $\kappa - \epsilon$ right.

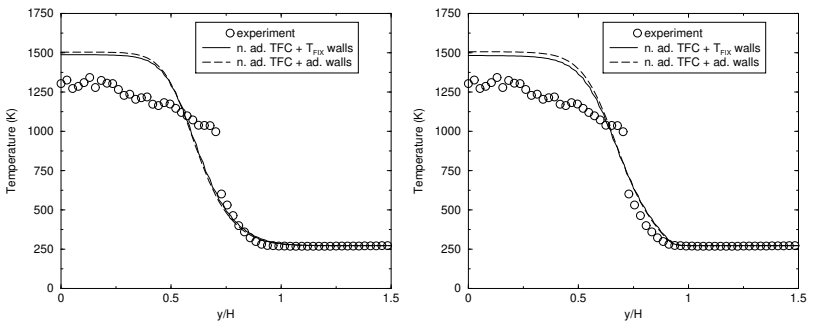

Figure 39: Adiabatic vs non adiabatic wall conditions: temperature distribution at $x/H = 1.04167$; $\kappa - \epsilon$ left; RNG $\kappa - \epsilon$ right.

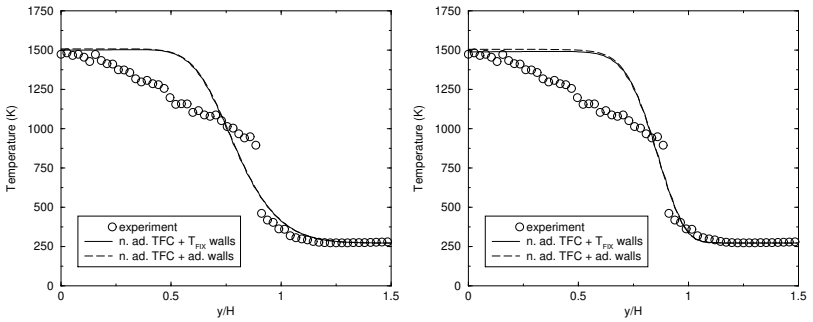

Figure 40: Adiabatic vs non adiabatic wall conditions: temperature distribution at $x/H = 3.125$; $\kappa - \epsilon$ left; RNG $\kappa - \epsilon$ right.

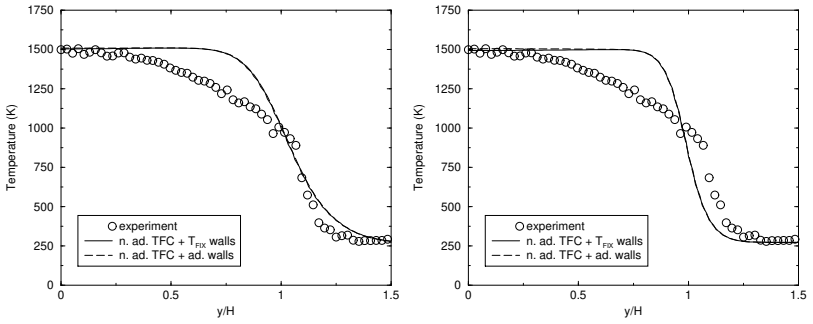

Figure 41: Adiabatic vs non adiabatic wall conditions: temperature distribution at $x/H = 6.25$; $\kappa - \epsilon$ left; RNG $\kappa - \epsilon$ right.

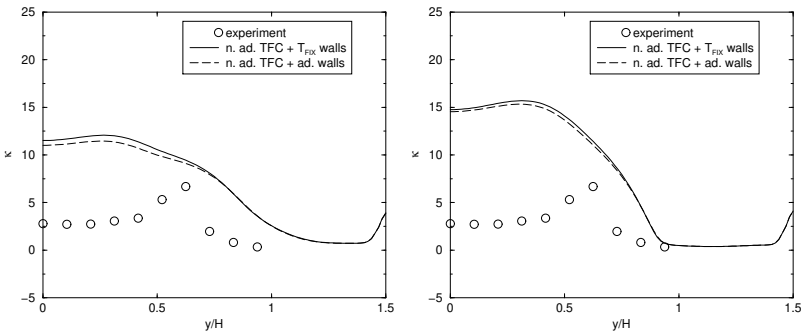

Figure 42: Adiabatic vs non adiabatic wall conditions: κ distribution at $x/H = 1.04167$; $\kappa - \epsilon$ left; RNG $\kappa - \epsilon$ right.

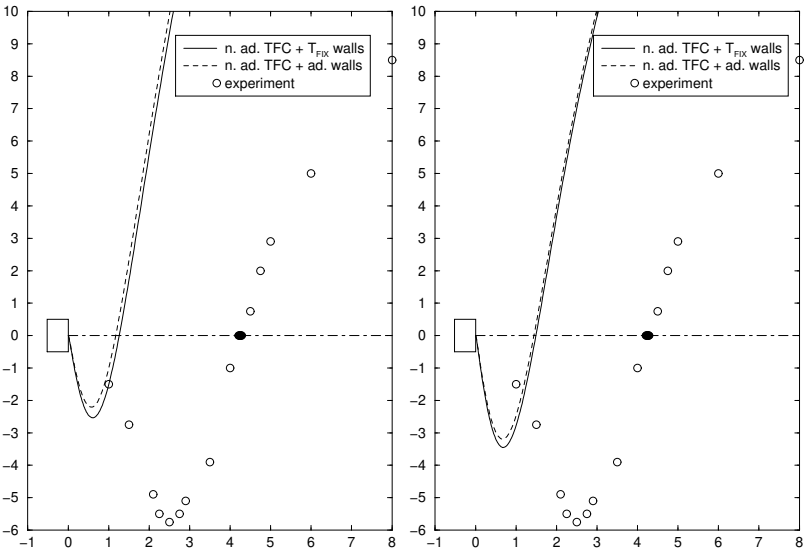

Figure 43: Adiabatic vs non adiabatic wall conditions: x-velocity distribution along the combustor axis; $\kappa - \epsilon$ left; RNG $\kappa - \epsilon$ right

6 Sensitivity to turbulence models

Analysis of the results obtained so far has put in evidence that:

- the non adiabatic formulation of the TFC model helps in obtaining a slightly more correct description of the velocity fields;
- more accurate results in terms of velocity component profiles could be achieved by using the RNG $\kappa - \epsilon$ turbulence model, which gives a better evaluation of the turbulent kinetic energy field, and a far better evaluation of the dimension of the ricirculating region behind the obstacle;
- **Ares** performs better than **Fluent** in genaral, and particularly better when adopting the RNG standard $\kappa - \epsilon$ model.

It seemed worthy to verify whether a further improvement of the results accuracy could be achieved by using a second order closure turbulence model, such as the Reynolds Stress Model (RSM), which is also available in Fluent.

The figures 47, 48 and 49 show a dramatic improvement of the results in terms both of the longitudinal and transversal velocity components.

The RSM model is the only one which is able to give the correct, even still qualitative, transversal velocity profile at the section $x/H = 1.04167$. The agreement with the experimental values becomes good also in quantitative terms at the two sections further downstream the channel. As a consequence, also the longitudinal velocity distribution along the channel axis, as shown in figure 50, is more correctly simulated, even though the length of the recirculation zone is still underestimated.

The figure 50 also shows the turbulent kinetic energy distribution at the section $x/H = 1.04167$, and gives reason why the RSM model is able to provide better results in terms of velocity fit. The actual turbulent kinetic energy distribution is far better captured by the RSM model, both from a quantitative and qualitative point of view. The computed κ distribution fits the experimental data from about $y/H = 0.7$ on, and it appears to be in fairly good qualitative accordance for values of $y/H < 0.7$, whereas the $\kappa - \epsilon$ family models do fail. The only RNG $\kappa - \epsilon$ model gives a somehow qualitative accordance with the experimental data in the range of $y/H > 0.7$.

The figures 44 to 46 show the computed temperature profiles at the usual sections. At the section $x/H = 1.04167$, the maximum temperature value which was

computed by using the RSM model is equal to about 1460 K, providing an extra gain of around 30 K on the value which was computed by using the RNG $\kappa - \epsilon$ model. As a general comment, the temperature gradient appears better resolved by the RSM model at all the examined locations, even the width of the burned zone seems underestimated, especially at the section $x/H = 6.25$.

A more accurate tuning of the TFC model parameters could most probably fix this discrepancy. Because the aim of the present computation was only to give a somehow quantitative measure of the influence of the turbulence modeling on the quality of the results, it has not been considered relevant to further investigate the matter.

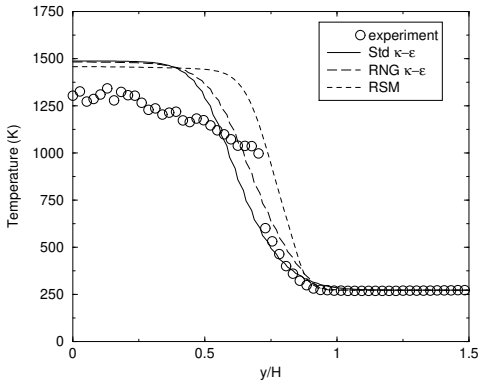

Figure 44: Temperature profile at $x/H = 1.04167$.

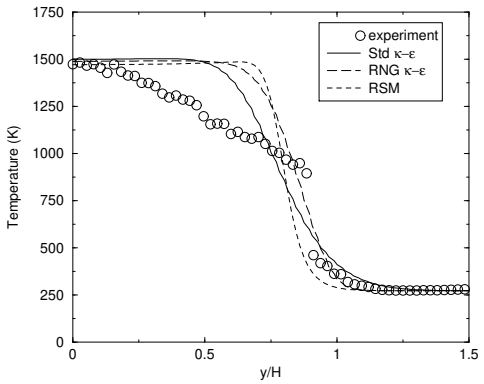

Figure 45: Temperature profile at $x/H = 3.125$.

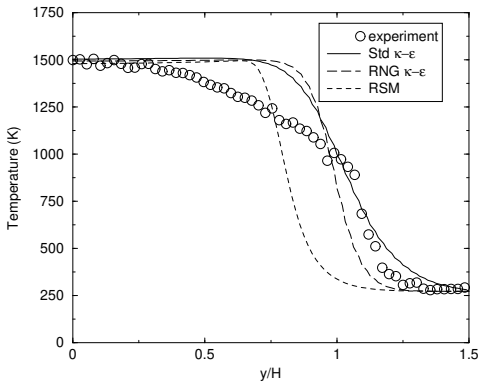

Figure 46: Temperature profile at $x/H = 6.25$.

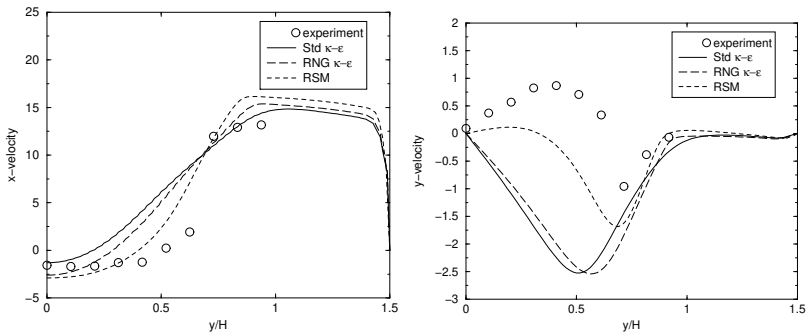

Figure 47: $x/H = 1.04167$: x-velocity distribution (left); y-velocity distribution (right).

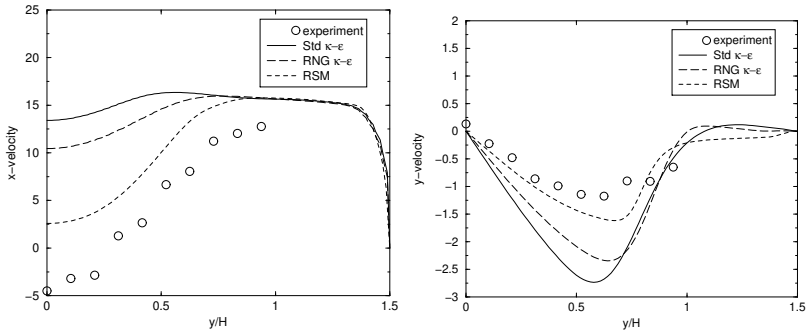

Figure 48: $x/H = 3.125$: x-velocity distribution (left); y-velocity distribution (right).

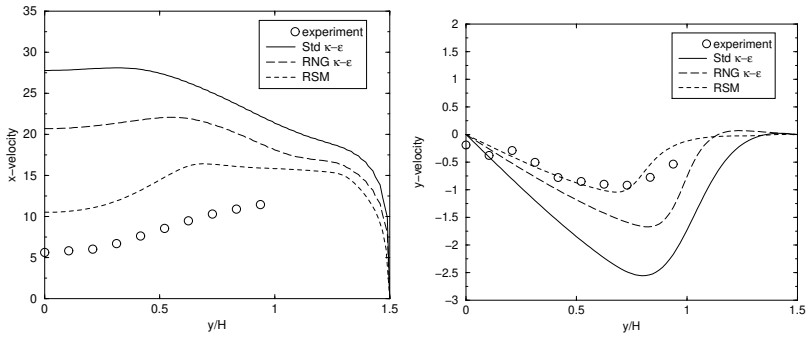

Figure 49: $x/H = 6.25$: x-velocity distribution (left); y-velocity distribution (right).

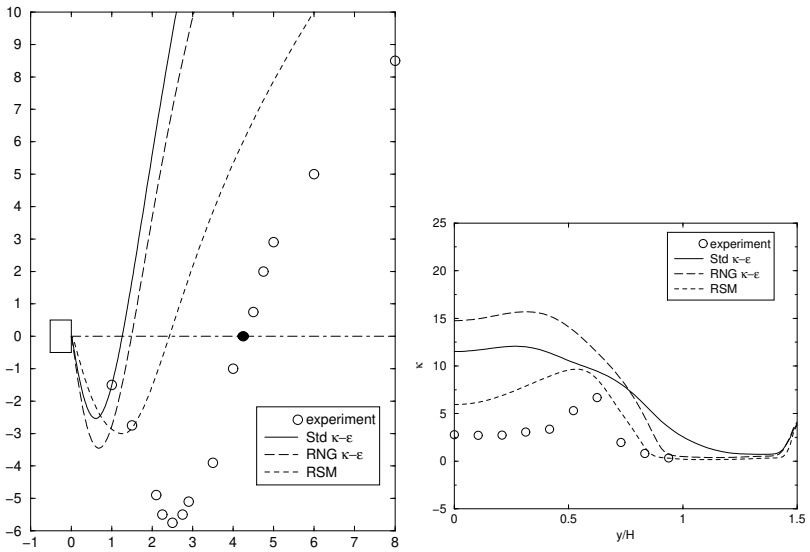

Figure 50: x-velocity distribution along the channel axis (left); turbulent kinetic energy distribution at $x/H = 1.04167$ (right).

7 Conclusions

The presented work had started from the attempt of simulating the premixed reactive flow in the experimental ENSMA combustor, by using the TFC premixed combustion model. The apparently simple test case had soon appeared to be a very tough one instead, challenging the two codes used (**Ares** and **Fluent**) and making very difficult to find good agreement with the experiemental measures.

The difficulties encountered were related to the TFC combustion model and to the turbulence model as well. The investigations carried out with the two codes put in evidence the need for extending the TFC model to non-adiabatic and heat-conducting capabilities. This work will be done during the third year of the project, re-designing the activities of Objective no. 8.

A strong effect due to the turbulence models was also found. **Ares** results were better then **Fluent** ones, whenever a comparison with the same turbulence model was possible. The best solution was found with RNG $\kappa - \epsilon$ model implemented into **Ares**, slightly better than **Fluent** results with a full Reynolds Stress Model.

References

[1] Stalio E. Mulas M. and Talice M. "Development and Implementation of Turbulence Models in the Combustion Code Ares". Technical Report CRS4-TECH-REP-00/95, CRS4 Research Centre, November 2000.

[2] Talice M. and Mulas M. "Development of a Partially Premixed Combustion Model". Technical Report CRS4-TECH-REP-01/54, CRS4 Research Centre, March 2001.

[3] *First European Test for Combustion Modelling Workshop*. Aussois, France, February 5-10, 1995.

[4] Zimont, V.L., Polifke, W., Bettelini, M. Weisenstein W. An Efficient Computational Model for Premixed Turbulent Combustion at High Reynolds Numbers Based on a Turbulent Flame Speed Closure. *Journal of Engineering for Gas Turbines and Power*, 120, July 1998.

[5] V. Zimont and M. Barbato. "Premixed and Partially Premixed Turbulent Combustion: Theory and Modelling". Technical Report CRS4-TECH-REP-97/71, CRS4 Research Centre, October 1999.

[6] Fluent Inc. *Fluent 5 User's Guide*. Fluent Inc., 1998.